Article:
Bonneville, S, Bray, AW and Benning, LG (2016) Structural Fe(II) oxidation in biotite by an ectomycorrhizal fungi drives mechanical forcing. Environmental Science & Technology, 50 (11). pp. 5589-5596. ISSN 0013-936X

https://doi.org/10.1021/acs.est.5b06178

Structural Fe(II) oxidation in biotite by an ectomycorrhizal fungi drives mechanical forcing

STEEVE BONNEVILLE[1*], *ANDREW W. BRAY*[2], *LIANE G. BENNING*[2, 3]

[1] Biogéochimie et Modélisation du Système Terre, Département Géosciences, Environnement et Société, Université Libre de Bruxelles, 50 av. F. D. Roosevelt, 1050 Brussels, Belgium

[2] Cohen Geochemistry, School of Earth and Environment, University of Leeds, LS2 9JT, United Kingdom.

[3] GFZ, German Research Centre for Geosciences, Telegrafenberg, Potsdam 14473, Germany.

ABSTRACT Microorganisms are essential agents of Earth's soil *weathering engine* who help transform primary rock-forming minerals into soils. Mycorrhizal fungi, with their vast filamentous networks in symbiosis with the roots of most plants can alter a large number of minerals via local acidification, targeted excretion of ligands, submicron-scale biomechanical forcing and mobilization of Mg, Fe, Al and K at the hypha-biotite interface. Here, we present experimental evidence that *Paxillus involutus* –a basidiomycete fungus- in ectomycorrhizal symbiosis with Scots pine (*Pinus sylvestris*), is able to oxidize a substantial amount of structural Fe(II) in biotite. Iron redox chemistry, quantified by X-ray Absorption Near Edge Spectra on 13 fungi-biotite sections along three distinct hypha colonizing the [001] basal plane of biotite, revealed variable but extensive Fe(II) oxidation up to ~ 2µm in depth and a Fe(III)/Fe_{total} ratio of up to ~0.8. The growth of Fe(III) hydroxide implies a volumetric change and a strain within the biotite lattice potentially large enough to induce micro-crack formation, which are abundant below the hypha-biotite interface. This Fe(II) oxidation also leads to the formation of a large pool of Fe(III) (i.e., structural Fe(III) and Fe(III) oxyhydroxides) within biotite that could participate in the Fe redox cycling in soils.

TOC/ABSTRACT ART

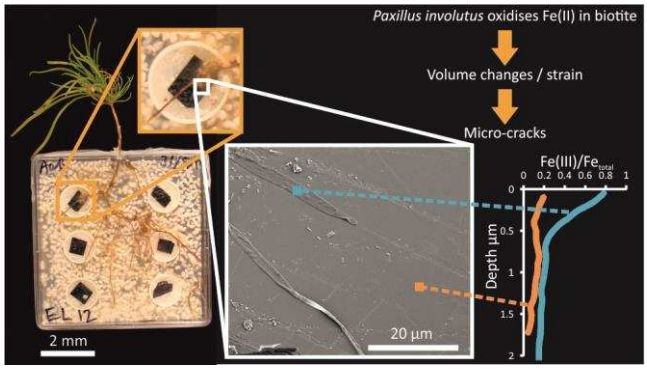

38 **INTRODUCTION**

39 Fungi represent a substantial portion of Earth's biosphere. In soils, they play a significant role in
40 the weathering of primary rock-forming minerals into secondary clay minerals [1]. The symbiosis
41 (i.e., mycorrhiza) that fungi can form with the root system of most plants - 80% of land plant
42 species [2,3] – is sustained by a substantial fraction (up to 30%) of net photosynthesis [4]. This
43 energy supply from the host plant sustains a massive network of microscopic filaments -hypha-
44 which can reach 200 m cumulative length per gram of soil, a much larger interfacial reactive
45 surface with the soil environment than plant rootlets [4]. A series of recent experimental studies
46 have pushed the notion that the fungal biomass can enhance weathering of rocks or minerals
47 commonly found in soils. These include biotite[5], chlorite [6], apatite [7] and rocks such as limestone,
48 basalt and gabbro [8], however this has been questioned for apatite in a field study [9].

49 Two of the most common rocks, granite and basalt, that represent the bulk of the continental and
50 oceanic crusts, are Fe rich. Most of the Fe contained in their constitutive primary minerals,
51 including biotite, is in the ferrous form, Fe(II). When exposed to the oxidative conditions at the
52 Earth's surface, this structural Fe(II) tends to oxidize and due to their low solubility readily
53 precipitate as various, most often poorly ordered Fe(III) oxyhydroxides. Biotite belongs to the
54 Fe(II)-rich phyllosilicates within the mica group and forms a solid-solution series between an
55 iron-end member, annite, and the magnesium-rich phlogopite. As one of the three main
56 constituents of granite, biotite is widespread at the Earth' surface where it represents ~7% of the
57 exposed continental crust [10]. Experiments of biotite weathering in aqueous solution[11,12], in
58 presence of bacteria[13], in interaction with fungi alone[14] or in symbiotic association with plant
59 roots [5,15] have all shown that this mineral can be a source of K, Mg, Al and Fe which are

60 potentially bioavailable for soil biota. The abiotic aqueous weathering sequence of biotite, is
61 dominated in the first stages by the release of interfoliar K [16,17]. This triggers its transformation
62 towards vermiculite, while the structural Fe(II), mainly in the octahedral sheets, is oxidized into
63 Fe(III)[18].

64 Soil biota have the potential to enhance biotite weathering. Roots, bacteria and fungi can indeed
65 modify the chemical composition and lower the pH of fluids in their near-environment through
66 (i) the exudation of protons to balance for uptake of cations [19] and/or the (ii) production of
67 ligands and CO_2-producing dissimilatory reactions [20]. All of these biological processes will
68 enhance mineral dissolution reactions beyond the abiotic levels in the near-environments of
69 active microorganisms [5,8,21]. Bacteria have also been shown to affect the Fe redox state within
70 biotite. For example, nitrate-reducing bacteria can oxidize up to ~5% of the total structural Fe(II)
71 of biotite [22]. Similarly, *Shewanella putrefaciens* - a well known Fe(III) reducing bacteria [23] - can
72 reduce up to 36% of the initial Fe(III), which can account in itself for up to ~20% of the total Fe
73 in the biotite crystalline structure [24]. Early studies have also demonstrated the capacity of some
74 fungi species- mostly the nitrate-reductase inducible taxa- to reduce Fe(III) oxides [25].

75 However, very few studies focused on the oxidation potential of fungi towards Fe(II) or, for that
76 matter, of any other redox sensitive elements in the crystalline structures of minerals. Although,
77 several studies [26-28] have qualitatively assessed the oxidation of Fe(II) in biotite in the presence
78 of mycorrhiza, so far no quantification of the extent of such an Fe(II) oxidation or the
79 localization of an oxidative front are available. This is despite the fact that Fe oxidation reactions
80 often initiate mineral weathering i.e., when primary minerals interact first with oxygenated fluids
81 iron is one of the first and fastest reacting redox element often leading to the formation of poorly

soluble Fe(III) oxyhydroxides. Interestingly, the formation of secondary Fe(III) phases due to the oxidation of Fe(II)-bearing minerals including biotite and pyroxenes was shown to also increase strain (due to volumetric changes) within mineral lattice structures, leading to micro-crack formation [29-31]. Ultimately in soils, this phenomenon increases porosity, allowing for water infiltration, which further favors and enhances subsequent mineral dissolution. What is however, still unknown is what the role and effect of fungal colonization on the iron speciation in pristine Fe(II) rich minerals during weathering.

In this study, we measured the capacity of mycorrhizal fungi to oxidize structural Fe(II) in biotite that was colonized by fungal networks in plant-mycorrhiza-mineral continuum systems. We quantified submicron-scale changes in ferric to total iron ($Fe(III)/Fe_{total}$) speciation and complemented these measurements with assessments of changes in C-rich compounds at the interface between ectomycorrhizal hypha and the basal [001] plane of biotite. With this study, we do not only provide a first comprehensive and spatially-resolved high resolution dataset of fungal Fe(II) oxidation of a Fe-rich silicate minerals in close-to-natural conditions, but we also elucidate whether the presence of Fe(III) oxides sub-domains can cause strain and mechanical forcing of the biotite crystalline structure, which in turn leads to further weathering.

MATERIALS AND METHODS

Microcosm setup. Biotite mycorrhizal weathering experiments were carried out in monoxenic microcosms following the methods described in [5,27,32] (Fig. 1). Briefly, *Paxillus involutus* – an ectomycorrhizal fungi- and *Pinus sylvestris* - Scots pine- were initially grown separately, then both transferred into the same Petri dish to initiate symbiosis. Symbiotic pairs were subsequently transferred into experimental microcosms, where freshly-cleaved biotite flakes (~ 0.5 X 0.5 cm

104 and 1 mm thick, positioned away from roots) were the main source of nutrients (i.e., K, Mg, Fe)
105 as illustrated in Fig. 1A. Microcosms were incubated for ~4 months at 15°C (days) and 10°C
106 (nights) with an 18h photoperiod with a photon flux density of 550 µmol m^{-2} s^{-1} following the
107 methods described previously [5,27].

108 *Sampling of hypha-biotite interface*. Three biotite flakes colonized by mycelia connected to the
109 plant roots however not in contact with the rootlets were collected from three different
110 microcosms. The separated biotite-fungal samples were sectioned using a Focus Ion Beam (FIB,
111 dual beam FEI Nova 200 NanoLab) following the procedure described in Bonneville et al.
112 (2009). In each sample, 3-4 sections were cut along single, isolated and continuous hypha (700 to
113 900 µm long). Sections were cut starting in each case from the tip (Fig 1B) and progressing away
114 from the tip (Fig 1C) to obtain a time sequence of exposure. On each biotite surface at least ~100
115 µm away from any hypha a control section was also cut. In total, 13 ultrathin FIB sections along
116 three hyphae ('A', 'B' and 'C') starting from the fungal tip towards the older parts were prepared
117 (Table S1). These FIB sections were subsequently imaged and analysed using Transmission
118 Electron Microscopy (TEM) as described in Bonneville et al. [27] and spectrally analysed using
119 Scanning Transmission X-ray Microscopy (STXM).

120 *Carbon, potassium, and ferrous/ ferric iron ratio mapping*. STXM mapping and collection of X-
121 ray Absorption Near Edge Spectra (XANES) at the Fe $L_{2,3}$ edges (700 – 730 eV) and for both C
122 K-edge and K $L_{2,3}$ edges (between 285 and 305 eV) were performed on all 13 FIB sections either
123 at the PolLux beamline (Swiss Light Source) or at beamline 5.3.2 at the Advanced Light Source
124 (USA).

Monochromatic X-rays focused on the sample using a Fresnel zone plate were used to collect 2-D images by scanning the sample stage at a fixed energy with a spot size of ~40 nm. Combining the images from each energy steps (0.1 eV in fine regions or 0.25/0.5 eV in pre- or post-edge) produced 3D image 'stacks' of the differential absorption of X-rays of the FIB sections. XANES line-scans were also acquired across the hypha-biotite interface. Maps of Fe(III)/Fe_{total} ratios, as well as maps of potassium and of the various carbon functional groups were acquired and processed [33]. To quantify the Fe speciation in linescans (with aXis 2000) and stacks (with Matlab routines), Singular Value Decomposition was performed using Fe(II) -siderite- and Fe(III) –goethite- as reference spectra. For C, the peak area at 285.4 eV (due to the transition C 1s → π* (* excited states) of the sp^2 hybridized carbon (i.e., C=C bonds), the peak at 288.5 eV characteristic of the C 1s → $\pi^*_{-(C^*=O)OH}$ transition for –COOH groups [33,34] were integrated (Fig. S-1). Fe and C-related Matlab scripts are available online from [35] and [36] respectively. All STXM measurements were performed with dwell times of <3.5 ms (per energy step per pixel), which was shown to induce negligible Fe(II) oxidation due to X-ray beam damage in chlorite, a phyllosilicate closely related to biotite [37].

RESULTS AND DISCUSSION

Our data shows that at or close to the contact with ectomycorrhizal hypha, structural Fe(II) oxidation was extensive in the biotite. Control sections had an average Fe(III)/Fe_{total} ratio of ~ 0.17 ± 0.06 SD (n = 53) with values ranging from 0.04 to 0.26 (Fig. S-2 for control FIB section corresponding to hypha 'A'). These are in line with bulk Fe(III)/Fe_{total} ratio of 0.175 reported for the Moen biotite [38]. The measured ranges of Fe(III)/Fe_{total} ratios highlights the inherent heterogeneous nature of the Fe valency within the biotite structure. Upon hypha colonization,

the biotite Fe(III)/Fe_{total} ratios increases by a factor of 3 to 5, reaching values up to ~0.8 under hypha 'B' and 'A' (near the interface with the hypha) and a value over 0.6 under hypha 'C' (Fig. 2). Despite the fact that Fe(II) oxidation was observed underneath all three hypha, the data revealed that the evolution and extent of this redox change along each hypha was quite variable. For instance in hypha 'A' (Fig. 2A), Fe(III)/Fe_{total} maps showed a TIP section underneath which, relative to the control section, little Fe(II) oxidation was observed (Fe(III)/Fe_{total} ratios between 0.05 and 0.35; Fig. S-2). In contrary, the section located ~300 μm away from the tip ('A' TIP+1) showed a larger Fe(II) oxidation with Fe(III)/Fe_{total} ratios of ~ 0.4-0.6. Interestingly, the 'A' TIP+2 section – the furthest away from the tip (~625 μm) - was slightly less oxidized than the middle section, with Fe(III)/Fe_{total} ratios between 0.25 – 0.5. For hypha 'B' and 'C', the trends of Fe(II) oxidation were different with the biotite beneath the tip being generally more oxidized than under the older sections of the hypha (Fig. 2A and 2B). When considering the Fe(III)/Fe_{total} depth profiles (Fig. 2), there is also a large variability from one FIB section to another regardless if the measurements were carried out on the same or on different biotite flakes. For example, TIP, TIP+2 and TIP+3 of hypha 'C' and TIP of hypha 'B' did not show variations with depth, while other sections (TIP+2 for hypha 'A', TIP+1 and TIP+2 for hypha 'B' and TIP+1 hypha 'C') showed an increase in the Fe(III)/Fe_{total} ratios towards the interface with the hypha (Fig. 2). On the contrary, two sections in hypha 'A' (TIP+1 and, to a lesser extent, TIP) showed a decrease in Fe(III)/Fe_{total} ratios towards the interfacial regions compared to deeper portion of the sections.

We interpret these discrepancies in the extent of Fe(II) oxidation to be the consequence of either differences in exposure time between the mineral and the hypha or in temporal variations in the biological activity of each hypha. It is worth noting that the tip of a hypha and, naturally its most

170 proximal region, are the most active both physiologically [39], and in terms of excretion [40]. Thus
171 these would be putatively the most 'active Fe(II) oxidizing' portion of the hypha. Apical growth
172 of hypha proceeds by sudden pulses irregularly spread in time and thus growth is far from
173 continuous [41]. This means that at any given point during the colonization of the biotite surface,
174 the period of interaction between the tip and the biotite surface (i.e., the time period when Fe(II)
175 oxidation occurs) can vary greatly. Thus, the $Fe(III)/Fe_{total}$ ratios in biotite do not necessarily
176 increase from the tip along the hypha. The depth profile of $Fe(III)/Fe_{total}$ in section TIP+1 'B' (
177 Fig. 2B) shows an increase from the structural value of ~0.2 at ~600 nm to a maximum of ~0.8 at
178 the hypha-mineral interface. This suggests that the Fe(II) oxidation process is mediated from the
179 interface with the hypha. Previous studies have already shown that the interfacial electron
180 transfer from reduced dissolved cations – such as Fe(II) – to micas and clay mineral surfaces
181 occur readily and are fast [42-44]. The electron hopping rate or the conductivity along octahedral
182 sheets (i.e., parallel to (001) plane) are fast in annite (10^6 s^{-1})[45] and nontronite (10^{-5} s^{-1})[46]. In the
183 latter, an electron would travel 0.5 µm in only 4 min along an octahedral sheet [46], however
184 electron transfer through tetrahedral sheets or across interfoliar space (perpendicular to (001)
185 plane) are much slower. For the Moen biotite (used in the present study), Rüscher and Gall[47]
186 report electrical conductivities (σ) perpendicular to (001) plane three orders of magnitude slower
187 than parallel to (001) plane, nevertheless the former was still measured to be ~ 10^{-13} $S.cm^{-1}$. The
188 same authors suggest that the conductivity perpendicular to (001) plane is controlled by defects
189 in the biotite lattice structure that create conducting bridges between T-O-T (tetrahedral-
190 octahedral-tetrahedral) layers. In Fig. 3D and also in Bonneville et al.[27] (in Fig. 3), numerous
191 micro-cracks and defects are visible to a depth of ~300 nm (and possibly deeper) in the biotite
192 lattice structure beneath hypha, we hypothesize that these defects facilitate the 'upward' electron

193 transfer and explain that substantial Fe(II) oxidation could affect 'deep' portions of the biotite
194 structure in the time-frame of the hyphal colonization.

195 A recent AFM study showed that *P. involutus* tips colonizing chlorite [001] basal plane grow on
196 a 40-80 nm thick layer of hydrated extracellular polymeric substances [48], which are also visible
197 in sections in Fig. 3C (arrows) and Fig. S-3. We suggest this 'biolayer' to be the location of the
198 oxidative compounds at the surface of the biotite. This is not surprising because our fungi
199 species, *P. involutus*, can secrete or express genes coding for various organic compounds
200 susceptible to oxidize Fe(II) such as laccase[49] and hydroxymate-bearing compounds[50].
201 Furthermore, during respiration, reactive oxygen species (ROS i.e., O_2-, H_2O_2 and $OH^{\cdot}$) can
202 easily be formed by the interaction of O_2 with common cellular constituents like flavoproteins
203 and quinones [51]. In most cases, ROS are quickly degraded back to O_2 by dismutase and catalase.
204 However, when excreted, ROS can have a profound effect on redox sensitive elements in the
205 hypha near-environment. For instance, *Stilbella aciculosa* (Ascomycete) is known to excrete O_2^-
206 that oxidizes dissolved Mn(II) leading to the precipitation of Mn(IV) oxide [52]. A recent study by
207 Keiluweit and coworkers[53] further demonstrates that the Mn(II) oxidative capability of fungi is
208 key to the long-term organic matter degradation in soils.

209 In the current study, we complemented the iron speciation measurements with μ-XANES
210 measurements at the C 1s edge to detect organic compounds potentially present within the biotite
211 or at the biotite-hypha interface (Fig. 4). To visualize this biotite-hypha boundary, the K maps of
212 the hypha 'A' sections are useful (Fig. 4, maps at right). For hypha 'B' and 'C', the Fe peak area
213 integrations were used to pinpoint the hypha-biotite interface in linescans (as illustrated in Fig.
214 S-2 for the control section sampled close to hypha 'A'). In our previous study[5], we showed that

215 Fe and K removal from biotite at the interface with hypha were only effective in the topmost 40
216 nm of the biotite in direct contact with the hypha. This is however also about the spatial
217 resolution of the STXM rastering images/linescans. Therefore, the interface between the Fe/K-
218 rich biotite and the K-'depleted' fungi appears here much less sharp (~150-200 nm in thickness
219 i.e. the equivalent of 3-4 pixels, Fig. 2 and Fig. 4). In addition, the biotite [001] basal planes were
220 probably not exactly parallel to the incident X-ray beam, and thus this misalignment effectively
221 enlarged the visualization of the physical hypha-biotite interface. The -C=C- maps (Fig. 4 at left)
222 show the opposite pattern to K, with no signals in the biotite and high levels in the fungi. Note
223 that the Pt layer deposited on top of the fungi during the FIB sectioning (~1.5 µm thick, see also
224 Fig. 2A) contains some O and is rich in C, originating from the precursor gas ($C_5H_5Pt(CH_3)_3$)
225 used for the Pt deposition process[54]. The Pt deposit makes a clear distinction of the hypha very
226 difficult in our chemical maps – however based on the process SEM images taken during the FIB
227 sectioning (not shown but see Fig. 1B), the hypha on top of biotite were about 250 nm thick and
228 thus this value was transferred also to the chemical maps reported in Fig. 2 and 4. The –COOH
229 maps show a weak to moderate signal in the biotite portions of the three FIB sections of hypha
230 'A' (Fig. 4). At first, we interpreted this –COOH signal within biotite to be due to electron/ion
231 beam induced deposition (E/IBID) during FIB sectioning [55]. However, the amorphous carbon
232 (graphite C) resulting from E/IBID would have given a signal of sp^2 hybridized carbon map,
233 which was not the case. This leaves open the possibility of –COOH containing compounds to be
234 present within the biotite as a result of hypha colonization. Further research is needed to
235 characterize *in situ* the composition of this hyphal 'biolayer' and its potential role in the fungal
236 weathering process.

237 The implications of this large biotite Fe(II) oxidation are far reaching in terms of fungal
238 weathering. Structural Fe(II) oxidation triggers (i) the loss of the Fe(III) from the octahedral
239 sheets concomitant with the conversion of coordinating hydroxyl into oxide groups, and as a
240 result (ii) the formation of amorphous Fe(III) oxides in the interlayer space [18,27,56-58]. The growth
241 of Fe(III) oxide subdomains in biotite imply a local increase in volume inducing strain in the
242 biotite lattice [29,30]. Structural defects in biotite lattices resulting from Fe(II) oxidation alone have
243 been also suggested [59]. Furthermore, according to Fletcher et al. [30], as biotite Fe(II) oxidation
244 proceeds and ferrihydrite is formed, elastic energy strain (per unit surface) accumulates until it
245 reaches values equivalent to the surface energy of fracture (2Γ – Table S2). Once this value is
246 reached, a crack forms. Interestingly, we showed previously [27], based on HR-TEM micrographs
247 of FIB section across similar hyphae-biotite interfaces, that the fungal colonization leads to a
248 substantial diffraction contrast (biotite crystal structure close to the interface was misorientated
249 by a 14° angle relative to bulk biotite) as well as numerous micro-cracks resulting from a
250 mechanical forcing of the biotite lattices. In some instances, rupture of the tetrahedra-octahedra-
251 tetrahedra (T-O-T) [001] biotite planes were associated with subdomains of ferrihydrite (Fig. 3D
252 in [27]). Such micro-cracks and diffraction contrasts were also observed in the FIB sections
253 described in the current study (e.g., Fig. 3D and Fig. S3). Using Fletcher's approach [30] (See
254 Supporting Information for calculation), we tested whether the elastic energy strain due to Fe(III)
255 hydroxide formation in biotite could trigger crack formation. Fletcher et al. [30] assumed that *all* of
256 the oxidized Fe(II) would form Fe(III) hydroxides within the biotite. This is questionable
257 because Rancourt et al. [57] showed (for annite) that Fe(III) hydroxides started to form only once
258 the $Fe(III)/Fe_{total}$ ratio reached a value of ~0.66 and that Fe(III) hydroxides represented *at*
259 *maximum* 11% of the total Fe in the phase. Using the 11% as a maximum value, we calculated

260 the threshold (2Γ) required for crack formation within the top ~30 nm of the oxidized biotite-
261 hyphae interface. In other words, when the Fe(III)/Fe_{total} exceeded the ratio of ~ 0.66 and
262 ferrihydrite made up 11% of the Fe_{total} in the biotite structure, the formation of micro-cracks at
263 ~30 nm intervals was feasible within an oxidation front progressing deeper into the biotite. The
264 calculated values are consistent with our observation of micro-cracks at depth within the biotite,
265 yet such micro-cracks were not systematically distributed or present in all FIB sections possibly
266 due to insufficient Fe(II) oxidation and Fe(III) hydroxides formation (Fig. 3D and Fig. S3).
267 Nevertheless, when present, these micro-cracks were not isolated and appeared in large numbers
268 even at depth corresponding to areas where large Fe(II) oxidation could still occur up to 200-300
269 nm from the interface with hypha (Fig. S-3). Although difficult to quantify, the formation of
270 such network of crack parallel to the [001] planes beneath the hypha and the secreted biolayer
271 resulting from extensive Fe(II) oxidation will likely weaken the overall cohesion of the biotite
272 and favor the exfoliation process (Fig. 3C and 3D). We also hypothesize that such crack
273 networks, when present, participate in the formation of channels beneath hypha once the
274 colonization of the biotite surface occurred (see in Fig. S-4 and [14]). Similar surface features were
275 reported as well in fungal weathering experiments with chlorite [6] and on muscovite in field
276 conditions [60]. Alternatively, the formation of a crack network could facilitate the penetration of
277 hypha within pre-existing fracture of the biotite surface (Fig. 5).

278 Although caution is required in extrapolating the results from our monoaxenic microcosms (free
279 of bacteria) to natural settings, the ability of common mycorrhiza to oxidize large amounts of
280 Fe(II) within the structure of biotite suggests that fungi could play an important role in Fe-
281 phyllosilicate redox cycling in soils. Indeed, Fe-phyllosilicates can serve both as electron donors
282 for Fe(II)-oxidizing microbial communities hence producing oxy-biotite or Fe(III) oxides [22] and

283 later as electron acceptors during dissimilatory Fe(III) reduction when anaerobic conditions may
284 develop in soils [24]. In contrast to microbial biotite Fe(II) oxidation, which forms limited amounts
285 of Fe(III) and which is coupled to NO_3^- reduction [22], the extent of mycorrhizal Fe(II) oxidation in
286 biotite is much larger (Fe(III)/Fe_{total} up to 0.8) and is fuelled (through mycelia growth) by the
287 photosynthetic activity of the host plants. More detailed studies on the coupling of mycorrhizal
288 and microbial processes in relation to phyllosilicate Fe redox cycling and weathering are
289 required to evaluate the significance of this phenomenon.

290

FIGURES

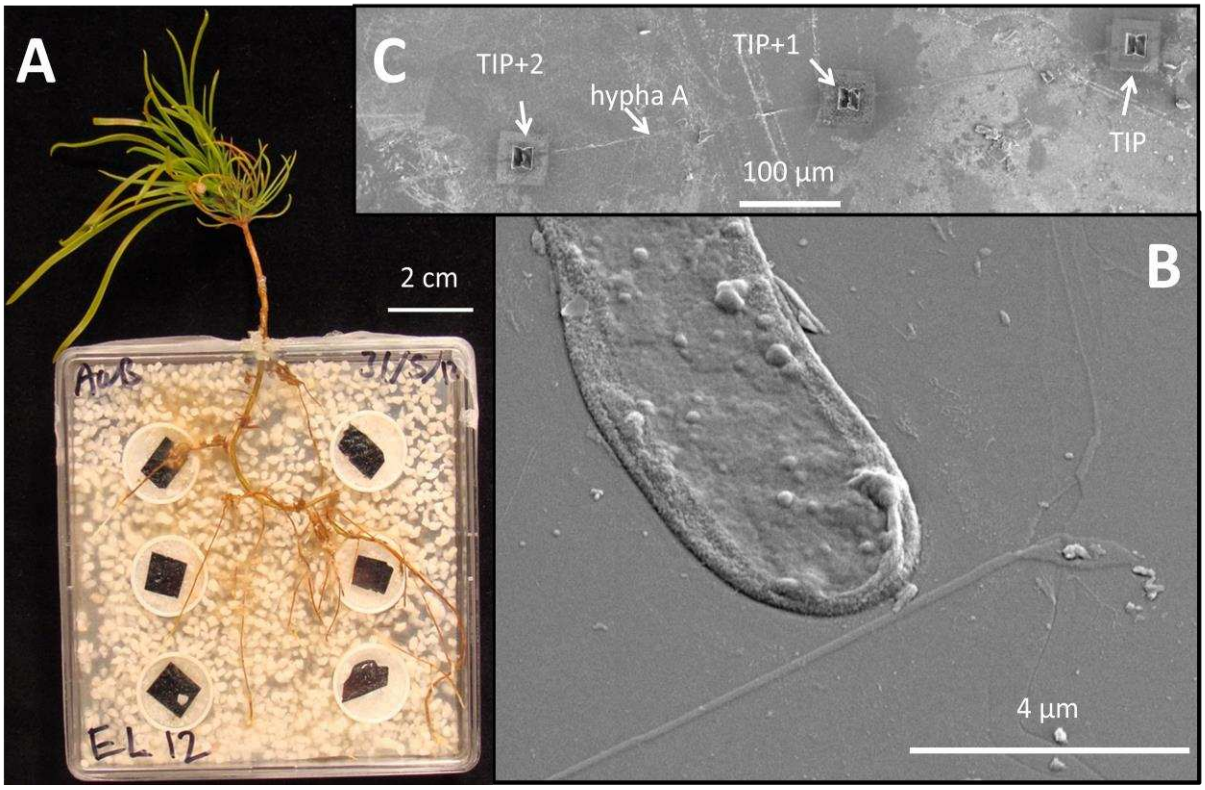

Figure 1: (A) Experimental microcosm after 4 months of growth. The mycelium that colonizes the biotite flakes appears as an orange haze around roots. (B) SEM micrographs of the tip of hypha 'A' before FIB milling respectively. (C) SEM micrographs of hypha 'A' sampled and of the three FIB sections.

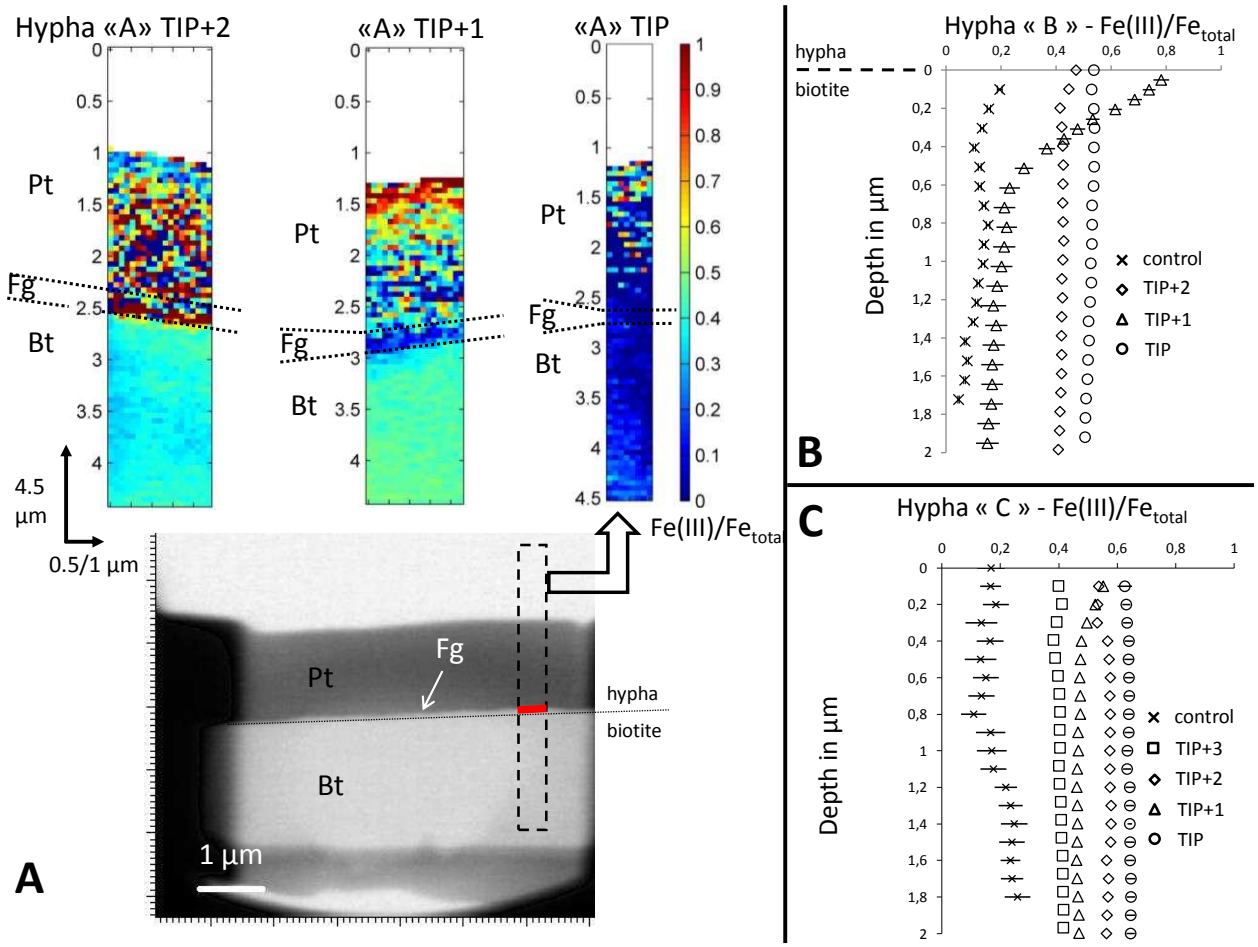

Figure 2: (A) Fe(III)/Fe$_{total}$ ratio maps in the three FIB sections cut along hypha 'A' with dashed lines highlighting the estimated position of the physical interfaces between fungi and biotite and between the fungi and the Pt deposit. Bottom image: red rectangle highlights the position of hypha analyzed in 'A' TIP. (B) and (C) depth profiles of Fe(III)/Fe$_{total}$ in the topmost 2 µm of biotite in contact with hypha or Pt deposit (controls) based on linescans (695-730 eV) on the FIB sections sampled on hypha 'B' and 'C'. (○) TIP FIB section; (△) TIP+1 FIB section; (◇) TIP+2 FIB section; (□) TIP+3 FIB section (only for hypha C).

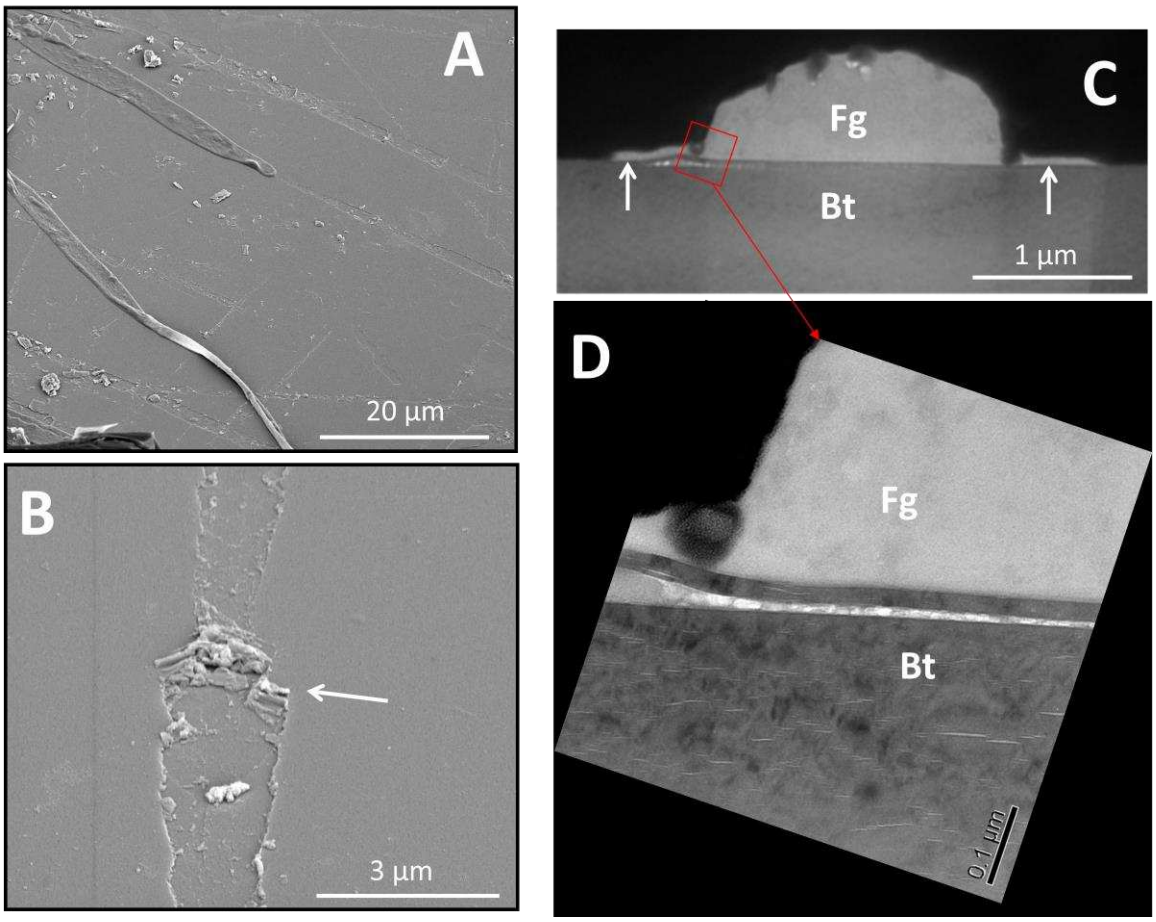

Figure 3: (A) SEM micrographs showing numerous channels (3-5 µm width) on the basal plane of biotite with (B) illustrating that some of the topmost biotite material is pushed away in the probable direction of hyphal pulsatile growth. (C) TEM bright-field micrographs of a FIB hypha-biotite section (not analyzed by XANES) showing a large crack near the interface with the hypha as well as an extensive "biolayer" (arrows) expanding from the central hypha. (D) Exfoliated layer and numerous micro-cracks at depth in the biotite. Note that all control FIB sections were free of such macro- and micro-cracks (see previous work [27] for detailed TEM observation of control sections)

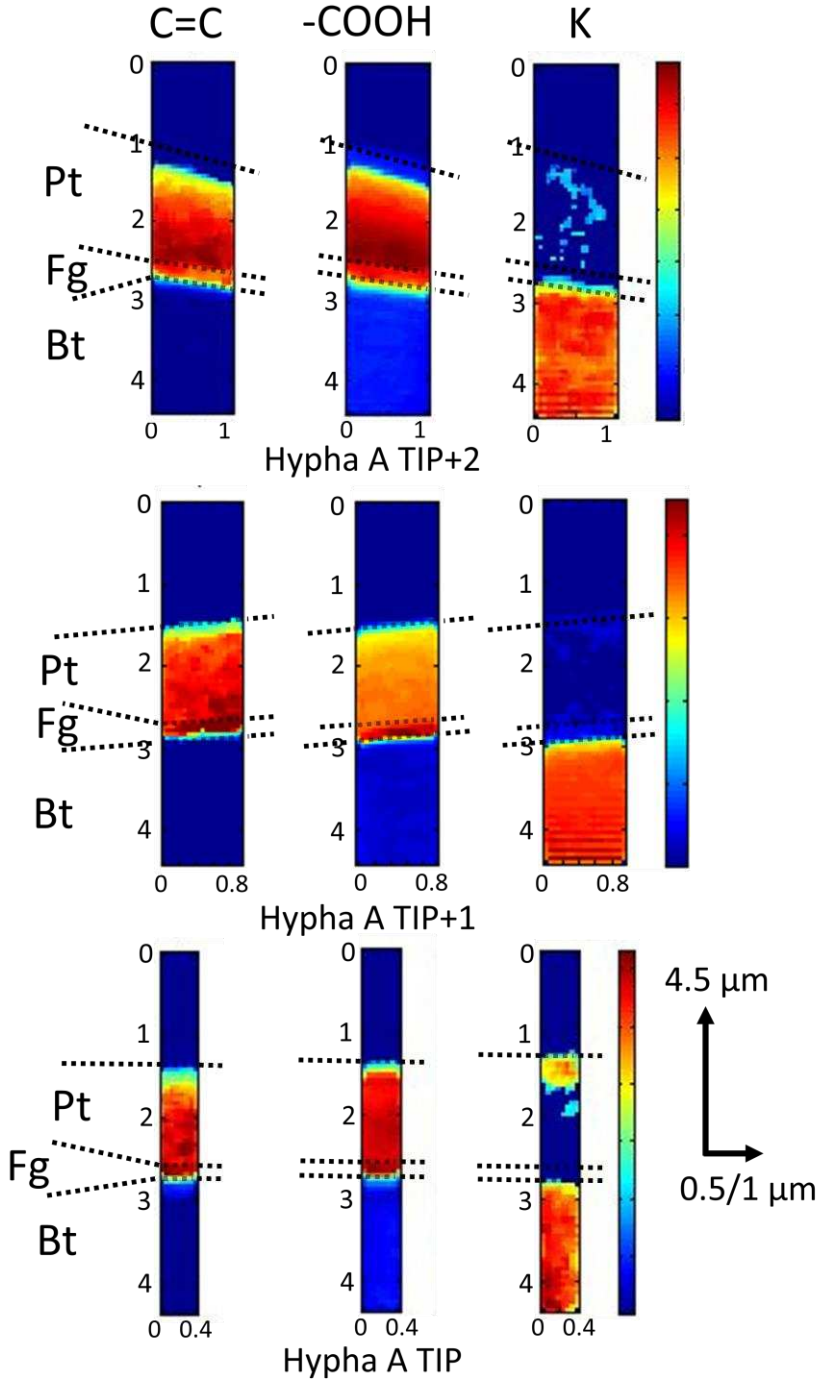

Figure 4: Abundance maps of sp^2 hydribized carbon (-C=C-), carboxyl carbon, and potassium in three FIB sections along hypha 'A'. Maps were calculated from peaks integration (see Fig. S-1). Numbers on axis are length and width in µm of the area analyzed.

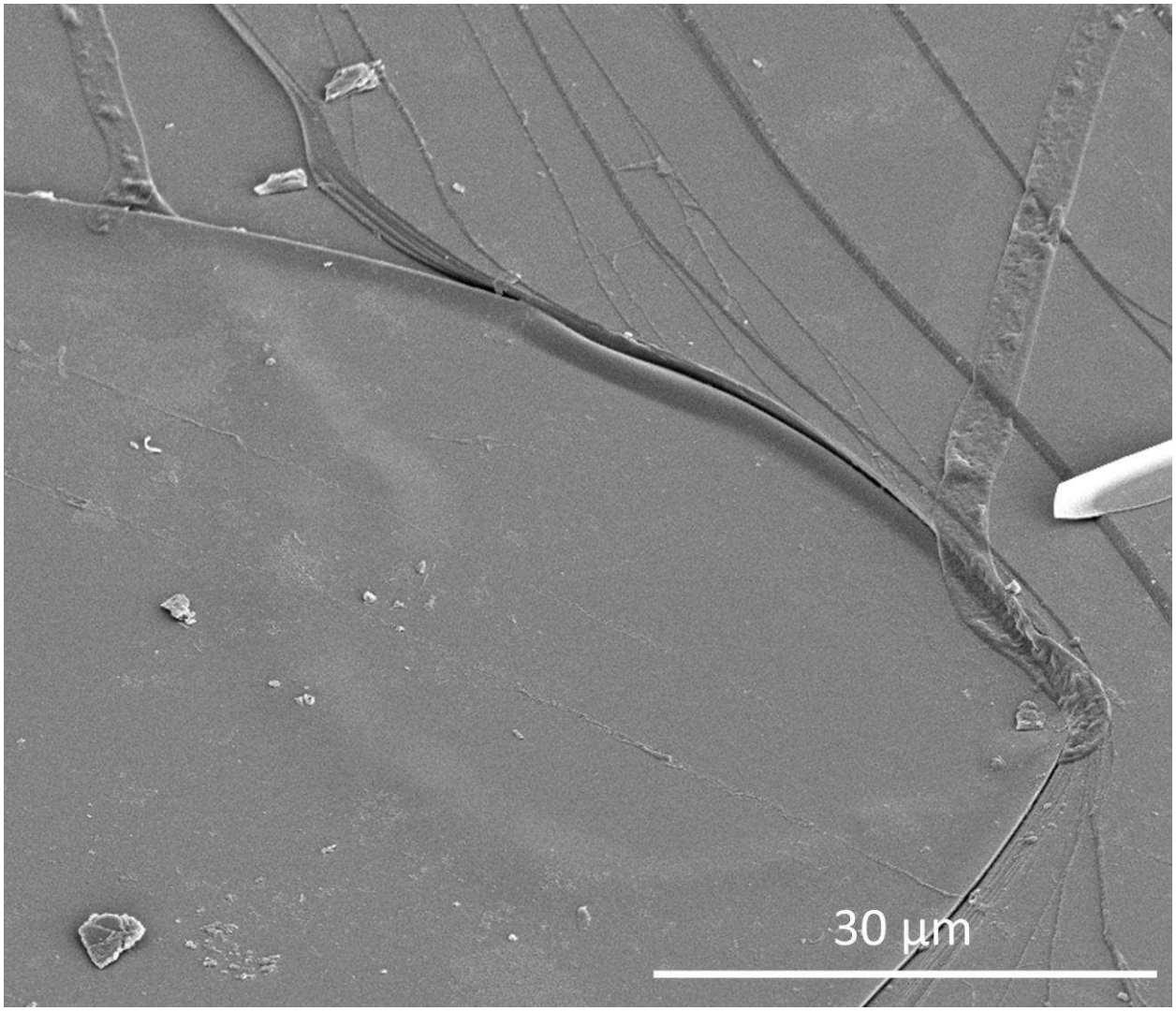

Figure 5 : SEM micrograph of an hypha that penetrated a pre-existing fracture on the biotite surface (top left and bottom right of the picture). This hypha has grown under the topmost layer of biotite as evidenced by the bulged aspect of the surface showing the probable pathway of the hypha within biotite.

ASSOCIATED CONTENT

Supporting Information. Include distances from tip of each FIB section sampled (Table S1), a description of the "biotite oxidation and ferrihydrite formation reactions scheme", as well as the details of "calculation of cracks calculation" with associated parameters (Table S2). This material is available free of charge via the Internet at http://pubs.acs.org.

AUTHOR INFORMATION

Corresponding Author

*Correspondence to : Steeve Bonneville (steeve.bonneville@ulb.ac.be) Biogéochimie et Modélisation du Système Terre, Département Géosciences, Environnement et Société, Université Libre de Bruxelles, 50 av. F. D. Roosevelt, CP160/02, 1050 Brussels, Belgium.

Author Contributions

The manuscript was written through contributions of all authors. All authors have given approval to the final version of the manuscript. S.B., A.W.B. and L.G.B. conceived the project, designed the study. S.B. carried out most of the data analysis and interpretation and wrote the manuscript.

ACKNOWLEDGMENT

D. Kylcoyne from the beamline 5.3.2 at Advanced Light Source (Lawrence Berkeley National Laboratory) are acknowledged for their help during STXM measurements. The Advanced Light Source is supported by the Director, Office of Science, Office of Basic Energy Sciences, of the U.S. Department of Energy under Contract No. DE-AC02-05CH11231. We acknowledge also the Paul Scherrer Institute, Villigen, Switzerland for provision of synchrotron radiation beamtime at beamline PolLUX of the Swiss Light Source and would like to thank J. Raabe for

assistance during STXM measurements. The authors thank John Harrington and Andy Brown and the Leeds Electron Microscopy and Spectroscopy Centre for help with the FIB sampling. A. Duran, M. Smits and J. Leake from the Department of Animal and Plant Sciences at the U. of Sheffield are acknowledged for their help during the microcosm experiments. SB thanks R. Behrends (GFZ Potsdam) for helpful discussions during the preparation of the manuscript. Funding from the UK Natural Environment Research Council "Weathering Science Consortium" grant NE/C004566/1 and a regular grant NE/J022365/1 to LGB are acknowledged. SB benefited also from the support of the "Victor Brien", "Van Buren" funds and the Fonds National de la Recherche Scientifique (FNRS –PDR T.1012.14).

REFERENCES

(1) Gadd, G. M. Geomycology: biogeochemical transformations of rocks, minerals, metals and radionuclides by fungi, bioweathering and bioremediation. Mycol. Res. **2007**, 111 (1), 3–49.

(2) Wang, B.; Qiu, Y.-L. Phylogenetic distribution and evolution of mycorrhizas in land plants. Mycorrhiza **2006**, 16 (5), 299–363.

(3) Smith, S. E.; Read, D. J. Mycorrhizal Symbiosis; Academic Press; Oxford, UK 2008.

(4) Leake, J.; Johnson, D.; Donnelly, D.; Muckle, G.; Boddy, L.; Read, D. Networks of power and influence: the role of mycorrhizal mycelium in controlling plant communities and agroecosystem functioning. Can. J. Bot. **2004**, 82 (8), 1016–1045.

(5) Bonneville, S.; Morgan, D. J.; Schmalenberger, A.; Bray, A.; Brown, A.; Banwart, S. A.; Benning, L. G. Tree-mycorrhiza symbiosis accelerate mineral weathering: Evidences from nanometer-scale elemental fluxes at the hypha–mineral interface. Geochim. Cosmochim. Acta **2011**, 75 (22), 6988–7005.

(6) S.A. Gazzè; Saccone, L.; Vala Ragnarsdottir, K.; Smits, M. M.; Duran, A. L.; Leake, J. R.; Banwart, S. A.; McMaster, T. J. Nanoscale channels on ectomycorrhizal-colonized chlorite: Evidence for plant-driven fungal dissolution. J. Geophys. Res. Biogeosciences **2012**, 117 (3) G00N09. DOI 10.1029/2012JG002016

(7) Smits, M. M.; Bonneville, S.; Benning, L. G.; Banwart, S. A.; Leake, J. R. Plant-driven weathering of apatite - the role of an ectomycorrhizal fungus: Plant-driven fungal weathering of apatite. Geobiology **2012**, 10 (5), 445–456.

(8) Schmalenberger, A.; Duran, A. L.; Bray, A. W.; Bridge, J.; Bonneville, S.; Benning, L. G.; Romero-Gonzalez, M. E.; Leake, J. R.; Banwart, S. A. Oxalate secretion by ectomycorrhizal Paxillus involutus is mineral-specific and controls calcium weathering from minerals. Sci. Rep. **2015**, 5. DOI 10.1038/srep12187

(9) Smits, M. M.; Johansson, L.; Wallander, H. Soil fungi appear to have a retarding rather than a stimulating role on soil apatite weathering. Plant Soil **2014**, 385 (1-2), 217–228.

(10) Nesbitt, H. W.; Young, G. M. Prediction of some weathering trends of plutonic and volcanic rocks based on thermodynamic and kinetic considerations. Geochim. Cosmochim. Acta **1984**, 48 (7), 1523–1534.

(11) Chae, G.-T.; Yun, S.-T.; Kwon, M.-J.; Kim, Y.-S.; Mayer, B. Batch dissolution of granite and biotite in water: Implication for fluorine geochemistry in groundwater. Geochem. J. **2006**, 40 (1), 95–102.

(12) Bray, A. W.; Oelkers, E. H.; Bonneville, S.; Wolff-Boenisch, D.; Potts, N. J.; Fones, G.; Benning, L. G. The effect of pH, grain size, and organic ligands on biotite weathering rates. Geochim. Cosmochim. Acta **2015**, 164, 127–145. DOI 10.1016/j.gca.2015.04.048

(13) Hopf, J.; Langenhorst, F.; Pollok, K.; Merten, D.; Kothe, E. Influence of microorganisms on biotite dissolution: An experimental approach. Chem. Erde - Geochem. **2009**, 69, 45–56.

(14) Balogh-Brunstad, Z.; Kent Keller, C.; Thomas Dickinson, J.; Stevens, F.; Li, C. Y.; Bormann, B. T. Biotite weathering and nutrient uptake by ectomycorrhizal fungus, Suillus tomentosus, in liquid-culture experiments. Geochim. Cosmochim. Acta **2008**, 72 (11), 2601–2618.

(15) Wallander, H.; Wickman, T. Biotite and microcline as potassium sources in ectomycorrhizal and non-mycorrhizal Pinus sylvestris seedlings. Mycorrhiza 9 (1), 25–32.

(16) Malmström, M.; Banwart, S. Biotite dissolution at 25 C: The pH dependence of dissolution rate and stoichiometry. Geochim. Cosmochim. Acta **1997**, 61 (14), 2779–2799.

(17) Bray, A. W.; Benning, L. G.; Bonneville, S.; Oelkers, E. H. Biotite surface chemistry as a function of aqueous fluid composition. Geochim. Cosmochim. Acta **2014**, 128, 58–70. DOI 10.1016/j.gca.2013.12.002

(18) Banfield, J. F.; Eggleton, R. A. Transmission electron microscope study of biotite weathering. Clays Clay Miner. **1988**, 36 (1), 47–60.

(19) Shen, J.; Tang, C.; Rengel, Z.; Zhang, F. Root-induced acidification and excess cation uptake by N 2-fixing Lupinus albus grown in phosphorus-deficient soil. Plant Soil **2004**, 260 (1-2), 69–77.

(20) Leyval, C.; Berthelin, J. Interactions between Laccaria laccata, Agrobacterium radiobacter and beech roots: Influence on P, K, Mg, and Fe mobilization from minerals and plant growth. Plant Soil **1989**, 117 (1), 103–110.

(21) Barker, W. W.; Welch, S. A.; Chu, S.; Banfield, J. F. Experimental observations of the effects of bacteria on aluminosilicate weathering. Am. Mineral. **1998**, 83, 1551–1563.

(22) Shelobolina, E.; Xu, H.; Konishi, H.; Kukkadapu, R.; Wu, T.; Blothe, M.; Roden, E. Microbial Lithotrophic Oxidation of Structural Fe(II) in Biotite. Appl. Environ. Microbiol. **2012**, 78 (16), 5746–5752.

(23) Bonneville, S.; Behrends, T.; Van Cappellen, P. Solubility and dissimilatory reduction kinetics of iron(III) oxyhydroxides: A linear free energy relationship. Geochim. Cosmochim. Acta **2009**, 73 (18), 5273–5282.

(24) Brookshaw, D. R.; Lloyd, J. R.; Vaughan, D. J.; Pattrick, R. A. D. Bioreduction of biotite and chlorite by a Shewanella species. Am. Mineral. **2014**, 99 (8-9), 1746–1754.

(25) Ottow, J. C. G.; Von Klopotek, A. Enzymatic reduction of iron oxide by fungi. Appl. Microbiol. **1969**, 18 (1), 41–43.

(26) Arocena, J. M.; Velde, B.; Robertson, S. J. Weathering of biotite in the presence of arbuscular mycorrhizae in selected agricultural crops. Appl. Clay Sci. **2012**, 64, 12–17.

(27) Bonneville, S.; Smits, M. M.; Brown, A.; Harrington, J.; Leake, J. R.; Brydson, R.; Benning, L. G. Plant-driven fungal weathering: Early stages of mineral alteration at the nanometer scale. Geology **2009**, 37 (7), 615–618.

(28) Smits, M. M.; Herrmann, A. M.; Duane, M.; Duckworth, O. W.; Bonneville, S.; Benning, L. G.; Lundström, U. The fungal–mineral interface: challenges and considerations of micro-analytical developments. Fungal Biol. Rev. **2009**, 23 (4), 122–131.

(29) Behrens, R.; Bouchez, J.; Schuessler, J. A.; Dultz, S.; Hewawasam, T.; Von Blanckenburg, F. Mineralogical transformations set slow weathering rates in low-porosity metamorphic bedrock on mountain slopes in a tropical climate. Chem. Geol. **2015**, 411, 283–298.

(30) Fletcher, R.; Buss, H.; Brantley, S. A spheroidal weathering model coupling porewater chemistry to soil thicknesses during steady-state denudation. Earth Planet. Sci. Lett. **2006**, 244 (1-2), 444–457.

(31) Jamtveit, B.; Putnis, C. V.; Malthe-Sørenssen, A. Reaction induced fracturing during replacement processes. Contrib. Mineral. Petrol. **2009**, 157 (1), 127–133.

(32) Smits, M. M.; Bonneville, S.; Haward, S.; Leake, J. R. Ectomycorrhizal weathering, a matter of scale? Mineral. Mag. **2008**, 72 (1), 131–134.

(33) Moffet, R. C.; Henn, T.; Laskin, A.; Gilles, M. K. Automated Chemical Analysis of Internally Mixed Aerosol Particles Using X-ray Spectromicroscopy at the Carbon K-Edge †. Anal. Chem. **2010**, 82 (19), 7906–7914.

(34) Keiluweit, M.; Bougoure, J. J.; Zeglin, L. H.; Myrold, D. D.; Weber, P. K.; Pett-Ridge, J.; Kleber, M.; Nico, P. S. Nano-scale investigation of the association of microbial nitrogen residues with iron (hydr)oxides in a forest soil O-horizon. Geochim. Cosmochim. Acta **2012**, 95, 213–226.

(35) http://www.mathworks.com/matlabcentral/fileexchange/24006-stxm-data-analysis-script-collection-stacklab.

(36) http://www.mathworks.com/matlabcentral/fileexchange/29085-stxm-spectromicroscopy-particle-analysis-routines.

(37) Bourdelle, F.; Benzerara, K.; Beyssac, O.; Cosmidis, J.; Neuville, D. R.; Brown, G. E.; Paineau, E. Quantification of the ferric/ferrous iron ratio in silicates by scanning transmission X-ray microscopy at the Fe L2,3 edges. Contrib. Mineral. Petrol. **2013**, 166 (2), 423–434.

(38) Ferrow, E. A. Experimental weathering of biotite, muscovite and vermiculite a Mössbauer spectroscopy study. Eur. J. Mineral. **2002**, 14 (1), 85–95.

(39) Deacon, J. Fungal Biology: 4th Edition; Blackwell Publishing ; 2013.

(40) Bartnicki-Garcia, S.; Bracker, C. E.; Gierz, G.; López-Franco, R.; Lu, H. Mapping the growth of fungal hyphae: orthogonal cell wall expansion during tip growth and the role of turgor. Biophys. J. **2000**, 79 (5), 2382.

(41) Lopez-Franco, R.; Bartnicki-Garcia, S.; Bracker, C. E. Pulsed growth of fungal hyphal tips. Proc. Natl. Acad. Sci. **1994**, 91 (25), 12228–12232.

(42) Alexandrov, V.; Neumann, A.; Scherer, M. M.; Rosso, K. M. Electron exchange and conduction in nontronite from first-principles. J. Phys. Chem. C **2013**, 117 (5), 2032–2040.

(43) Neumann, A.; Olson, T. L.; Scherer, M. M. Spectroscopic evidence for Fe(II)-Fe(III) electron transfer at clay mineral edge and basal sites. Environ. Sci. Technol. **2013**, 47 (13), 6969–6977.

(44) Schaefer, M. V.; Gorski, C. A.; Scherer, M. M. Spectroscopic evidence for interfacial Fe(II)-Fe(III) electron transfer in a clay mineral. Environ. Sci. Technol. **2011**, 45 (2), 540–545.

(45) Rosso, K. M.; Ilton, E. S. Charge transport in micas: The kinetics of FeII/III electron transfer in the octahedral sheet. J. Chem. Phys. **2003**, 119 (17), 9207–9218.

(46) Neumann, A.; Wu, L.; Li, W.; Beard, B. L.; Johnson, C. M.; Rosso, K. M.; Frierdich, A. J.; Scherer, M. M. Atom Exchange between Aqueous Fe(II) and Structural Fe in Clay Minerals. Environ. Sci. Technol. **2015**, 49 (5), 2786–2795.

(47) Rüscher, C. H.; Gall, S. On the polaron-mechanism in iron-bearing trioctahedral phyllosilicates: an investigation of the electrical and optical properties. Phys. Chem. Miner. **1995**, 22 (7), 468–478.

(48) Gazzè, S. A.; Saccone, L.; Smits, M. M.; Duran, A. L.; Leake, J. R.; Banwart, S. A.; Ragnarsdottir, K. V.; McMaster, T. J. Nanoscale Observations of Extracellular Polymeric Substances Deposition on Phyllosilicates by an Ectomycorrhizal Fungus. Geomicrobiol. J. **2013**, 30 (8), 721–730.

(49) Jacob, C.; Courbot, M.; Martin, F.; Brun, A.; Chalot, M. Transcriptomic responses to cadmium in the ectomycorrhizal fungus Paxillus involutus. FEBS Lett. **2004**, 576 (3), 423–427.

(50) Haselwandter, K.; Bobleter, O.; Read, D. J. Degradation of ^{14}C-labelled lignin and dehydropolymer of coniferyl alcohol by ericoid and ectomycorrhizal fungi. Arch. Microbiol. **1990**, 153 (4), 352–354.

(51) Aguirre, J.; Ríos-Momberg, M.; Hewitt, D.; Hansberg, W. Reactive oxygen species and development in microbial eukaryotes. Trends Microbiol. **2005**, 13 (3), 111–118.

(52) Hansel, C. M.; Zeiner, C. A.; Santelli, C. M.; Webb, S. M. Mn(II) oxidation by an ascomycete fungus is linked to superoxide production during asexual reproduction. Proc. Natl. Acad. Sci. **2012**, 109 (31), 12621–12625.

(53) Keiluweit, M.; Nico, P.; Harmon, M. E.; Mao, J.; Pett-Ridge, J.; Kleber, M. Long-term litter decomposition controlled by manganese redox cycling. Proc. Natl. Acad. Sci. **2015**, 112 (38), E5253–E5260.

(54) Vaz, A. R.; da Silva, M. M.; Leon, J.; Moshkalev, S. A.; Swart, J. W. Platinum thin films deposited on silicon oxide by focused ion beam: characterization and application. J. Mater. Sci. **2008**, 43 (10), 3429–3434.

(55) Randolph, S. J.; Fowlkes, J. D.; Rack, P. D. Focused, Nanoscale Electron-Beam-Induced Deposition and Etching. Crit. Rev. Solid State Mater. Sci. **2006**, 31 (3), 55–89.

(56) Farmer, V. C.; Russell, J. D.; McHardy, W. J.; Newman, A. C. D.; Ahlrichs, J. L.; Rimsaite, J. Y. H. Evidence for loss of protons and octahedral iron from oxidized biotites and vermiculites. Mineral. Mag. **1971**, 38, 119.

(57) Rancourt, D. G.; Mercier, P. H. J.; Cherniak, D. J.; Desgreniers, S.; Kodama, H.; Robert, J.-L.; Murad, E. Mechanisms and crystal chemistry of oxidation in annite: Resolving the hydrogen-loss and vacancy reactions. Clays Clay Miner. **2001**, 49 (6), 455–491.

(58) Murakami, T.; Utsunomiya, S.; Yokoyama, T.; Kasama, T. Biotite dissolution processes and mechanisms in the laboratory and in nature: Early stage weathering environment and vermiculitization. Am. Mineral. **2003**, 88 (2-3), 377–386.

(59) Kogure, T.; Nespolo, M. Atomic structures of planar defects in oxybiotite. Am. Mineral. **2001**, 86 (3), 336–340.

(60) Quirk, J.; Leake, J. R.; Banwart, S. A.; Taylor, L. L.; Beerling, D. J. Weathering by tree-root-associating fungi diminishes under simulated Cenozoic atmospheric CO_2 decline. Biogeosciences **2014**, 11 (2), 321–331.